



# Cross-bedding related anisotropy and its interplay with various boundary conditions in the formation and orientation of joints in an aeolian sandstone



Shang Deng<sup>a,\*,1</sup>, Antonino Cilona<sup>a</sup>, Carolyn Morrow<sup>b</sup>, Cesar Mapeli<sup>c</sup>, Chun Liu<sup>a</sup>, David Lockner<sup>b</sup>, Manika Prasad<sup>c</sup>, Atilla Aydin<sup>a</sup>

<sup>a</sup> Department of Geological and Environmental Sciences, Stanford University, Stanford, CA, USA

<sup>b</sup> US Geological Survey, Menlo Park, CA, USA

<sup>c</sup> Petroleum Engineering Department, Colorado School of Mines, Golden, CO, USA

## ARTICLE INFO

### Article history:

Received 7 November 2014

Received in revised form

30 April 2015

Accepted 6 May 2015

Available online 21 May 2015

### Keywords:

Cross-bed package confined joints

Joint zones

Cross-bed orientations

Interplay between rock anisotropy and strain boundary conditions

P-wave anisotropy

Aztec Sandstone

## ABSTRACT

Previous research revealed that the cross-bedding related anisotropy in Jurassic aeolian Aztec Sandstone cropping out in the Valley of Fire State Park, Nevada, affects the orientation of compaction bands, also known as anti-cracks or closing mode structures. We hypothesize that cross-bedding should have a similar influence on the orientation of the opening mode joints within the same rock at the same location. To test this hypothesis, we investigated the relationship between the orientation of cross-beds and the orientation of different categories of joint sets including cross-bed package confined joints and joint zones in the Aztec Sandstone. The field data show that the cross-bed package confined joints occur at high-angle to bedding and trend roughly parallel to the dip direction of the cross-beds. In comparison, the roughly N–S trending joint zones appear not to be influenced by the cross-beds in any significant way but frequently truncate against the dune boundaries.

To characterize the anisotropy due to cross-bedding in the Aztec Sandstone, we measured the P-wave velocities parallel and perpendicular to bedding from 11 samples and determined an average P-wave anisotropy to be slightly larger than 13%. From these results, a model based on the generalized Hooke's law for anisotropic materials is used to analyze deformation of cross-bedded sandstone as a transversely isotropic material. In the analysis, the dip angle of cross-beds is assumed to be constant and the strike orientation varying from 0° to 359° in the east ( $x$ ), north ( $y$ ), and up ( $z$ ) coordinate system. We find qualitative agreement between most of the model results and the observed field relations between cross-beds and the corresponding joint sets. The results also suggest that uniaxial extension ( $\epsilon_{zz} > \epsilon_{xx} = \epsilon_{yy} = 0$ ) and axisymmetric extension ( $\epsilon_{xx} = \epsilon_{yy} < \epsilon_{zz}$  and  $\epsilon_{xx} = \epsilon_{yy} > \epsilon_{zz}$ ) would amplify the influence of cross-bedding associated anisotropy on the joint orientation whereas a triaxial extension ( $\epsilon_{xx} > \epsilon_{yy} > \epsilon_{zz}$ ) would mitigate this influence. We suggest that the potential implication of different categories of joint sets (i.e., cross-bed package confined joints and joint zones) forming in response to the variation of the boundary conditions (axisymmetric extension and triaxial extension, respectively) and the interplay with the rock anisotropy is significant. These results have important implications for fluid flow through aeolian sandstones in reservoirs and aquifers.

© 2015 Elsevier Ltd. All rights reserved.

## 1. Introduction

Previous research documented the relationship between cross-bed orientation and the distribution of compaction bands in an aeolian sandstone (Deng and Aydin, 2012) and interpreted this relationship in terms of the strength anisotropy of localized compaction (Deng and Aydin, 2015). This research led to the notion that if the cross-bedding related anisotropy affects the orientation

\* Corresponding author. 450 Serra Mall, Building 320, Room 118, Stanford, CA, 94305, USA.

E-mail address: [shang.deng@alumni.stanford.edu](mailto:shang.deng@alumni.stanford.edu) (S. Deng).

<sup>1</sup> Now at ConocoPhillips Company, Houston, TX, USA.

of compaction bands, there is likely a similar effect on the formation and orientation of the joints that occur in the same rock at the same location. In comparison to compaction bands, joints are relatively simple structures that exhibit dominantly opening displacements across a plane of discontinuity (Pollard and Aydin, 1988). It has been frequently observed that joints generally occur perpendicular to bedding and are confined by layer boundaries or mechanical layer packages in sedimentary rocks (Hodgson, 1961; Price, 1966;

Hancock, 1985; Helgeson and Aydin, 1991; Narr, 1991; Gross and Engelder, 1995).

In this paper, we present the results of a multidisciplinary study integrating: (1) field data on the spatial relationship between joint sets and dune architectures including cross-beds and dune boundaries in the Aztec Sandstone; (2) laboratory measurements of the elastic moduli and P-wave anisotropy of the Aztec Sandstone, and (3) modeling the variation of the local principal stress

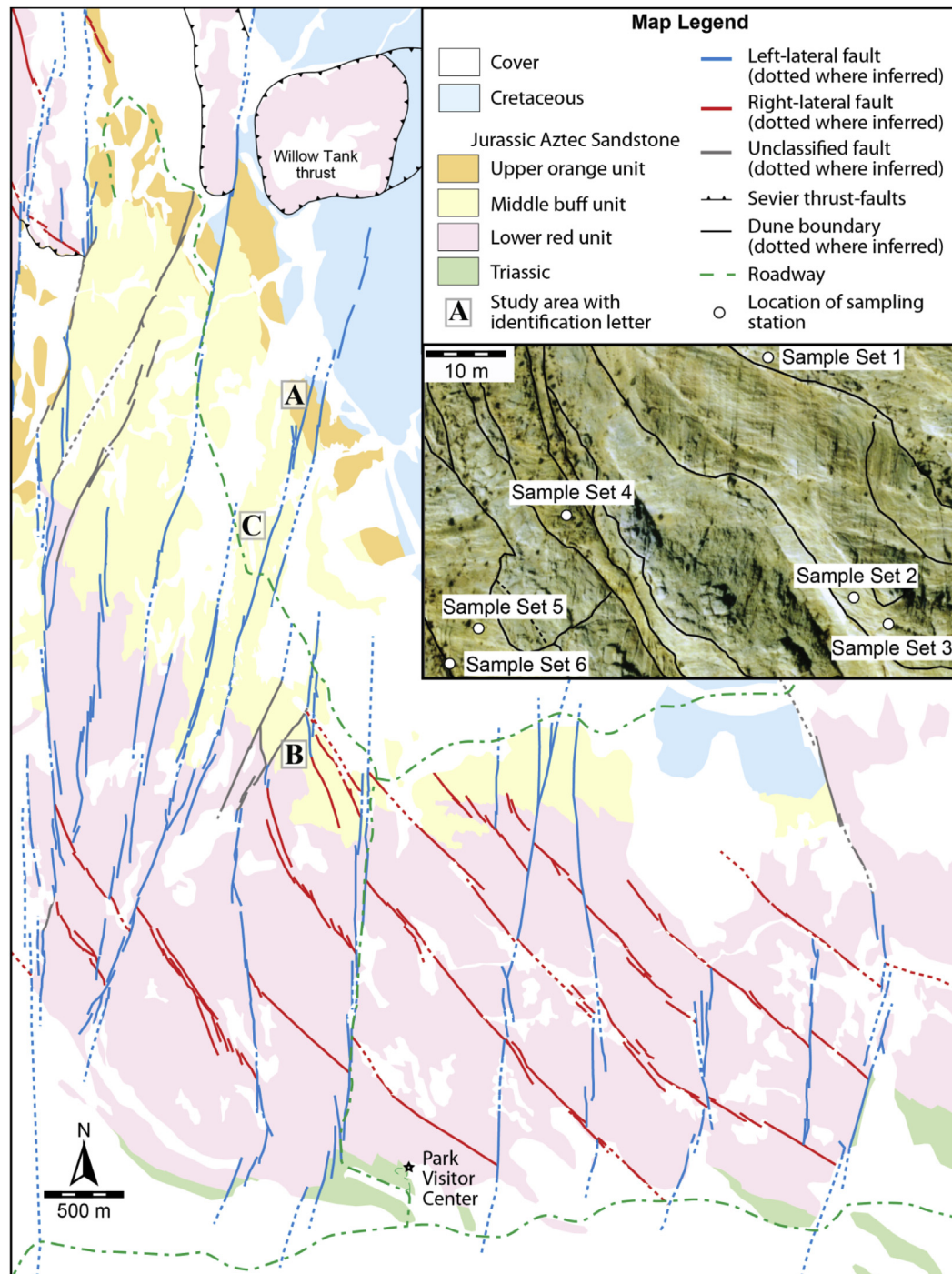


**Fig. 1.** Simplified geologic map of Valley of Fire State Park. Slightly modified from Flodin and Aydin (2004). The locations of the three study areas (sites A, B and C) and some other prominent geologic and geographic features are labeled. Locations of the sampling stations in Site C are shown on an enlarged aerial photograph in which the dune boundaries are labeled following Deng and Aydin (2012).

magnitudes and orientations in sandstone with cross-beds of different orientation under strain boundary conditions simulating various tectonic loadings. The objectives of the study are to decipher the relationship between the orientation of cross-beds and the presence and orientation of joints therein. In particular, we explore possible interplay between the anisotropy of the rock medium and the boundary conditions to which the medium is subjected, and the effect of such an interplay on the formation and orientation of joints. Ultimately, this new information is placed in a mechanical framework that may shed light on the formation and orientation of various types of joints in aeolian sandstones.

## 2. Geological setting

The Aztec Sandstone was deposited in a backarc basin tectonic setting during Early Jurassic time (Marzolf, 1983) and is interpreted to have formed along with the western margin of the Navajo-Nugget sand sea (McKee and Bigarella, 1979). Aeolian dunes in the Aztec Sandstone exposed in Valley of Fire State Park have medium to large-scale tabular-planar and wedge-planar cross strata truncated by widespread first-order and planar second-order bounding surfaces (Porter, 1987). The thickness of Aztec Sandstone varies across the Valley of Fire State Park with a maximum of about 1400 m (Bohannon, 1983). Due to multiple episodes of diagenetic alteration, the Aztec Sandstone is divided into three major alteration units: lower red, middle buff and upper banded orange units (Eichhubl et al., 2004).

The Aztec Sandstone was subjected to at least two significant deformation phases: (1) east-southeast-directed compressive deformation during the Sevier Orogeny of the late Mesozoic and (2) Basin and Range extension and strike-slip faulting primarily in mid-Miocene time and continuing to the present to a certain extent. Within the Valley of Fire State Park, deformation structures associated with the Sevier Orogeny are large-scale thrust faults (Bohannon, 1983), compaction bands and shear bands (Hill, 1989; Sternlof, 2006). Younger structures include approximately N–S oriented joint zones (Taylor et al., 1999), strike-slip faults and normal faults. In particular, Myer and Aydin (2004) recognized that the strike-slip faults and normal faults formed by shearing along pre-existing joints and joint zones. Flodin and Aydin (2004) documented that the fault arrays evolved by sequential opening-fracturing and shearing and resulted in the formation of a widespread strike-slip network including two fault sets with left-lateral and right-lateral slip. Recently, Aydin and de Jossineau (2014) proposed that the precursors of the strike-slip fault network were an array of relatively low-angle normal faults and their splay fractures.

In this study, two sets of orientation data for joints and cross-beds were collected primarily from the main study area (Site A in Fig. 1) located in the upper orange unit of the Aztec Sandstone. Some observations from Site B located in the middle buff unit are also used for the confirmation of the results drawn from Site A. Samples used to measure the elastic moduli and the P-wave anisotropy were collected from Site C (see inset in Fig. 1), which was the focus of the study for the previous research on the distribution and orientation of compaction bands (Deng and Aydin, 2012).

## 3. Methodology

In this study, mapping was carried out at scales ranging from 1:50 to 1:150 using enlarged aerial photographs taken at a height of about 20 m from a camera mounted on an unmanned aerial vehicle. Orientation measurements were collected using a Brunton compass. For all the measured structural orientation data, we use the right-hand-rule convention (Pollard and Fletcher, 2005).

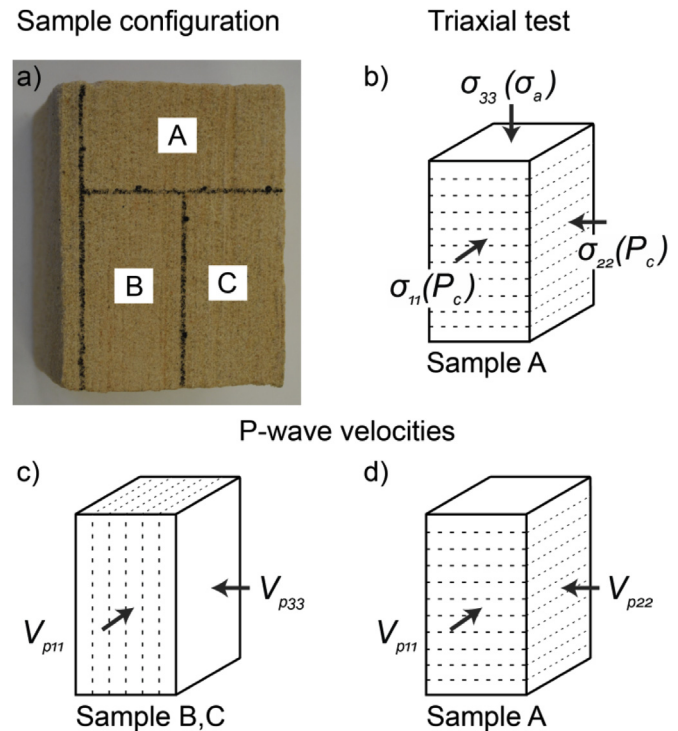


**Fig. 2.** Representative block samples (Set 3), triaxial test geometry and the velocities measured in the laboratory. a) Block samples with a layered texture collected from the field. The contour of the rectangular prism shaped samples used for triaxial tests and velocity measurements were defined with black lines. b) Configuration of sample A (bedding orientation are denoted by dashed lines) and the axisymmetric loading geometry. Axial load ( $\sigma_a$ ) is perpendicular to bedding. c) Configuration of samples B and C. P-wave velocities were measured parallel ( $V_{p22}$ ) and perpendicular to bedding ( $V_{p33}$ ). d) P-wave velocities measured in two orthogonal directions ( $V_{p11}$  and  $V_{p22}$ ) parallel to bedding on sample A.

To measure the elastic moduli and P-wave anisotropy of the cross-bedded sandstone, six blocks that showed no visible deformation features (i.e., deformation bands, joints or small faults) were sampled with care from fresh outcrops from four dune units in the field using hand saw blades. In the laboratory, each block was cut into a set of three rectangular prism shaped samples having one long axis and square cross section (Fig. 2a). The heterogeneity and the extreme friability of the sandstone made sample preparation challenging. Ideally, samples were prepared in the shape of rectangular prism with nominal cross sections of 25 by 25 mm and length of 50 mm, although individual sample dimensions varied. In each set of three samples (A, B and C), the long axis of sample A was oriented perpendicular to bedding whereas samples B and C had long axes parallel to bedding (Fig. 2a). This sample configuration was chosen to provide some level of redundancy in the bedding-parallel direction since there was obvious heterogeneity in properties due to cross-bedding at the sample scale. Following dry rough-cutting with a diamond saw, the final sample surfaces were refined by hand-sanding using 220 grit sandpaper on a flat surface. Sample ends were made parallel to each other within  $\pm 0.1$  mm, although corners and edges were typically rounded due to inevitable loss of grains during sanding. Following the preparation step, the sample dimensions were measured using a digital caliper with precision of 0.01 mm. Each measurement were repeated three times and the average values were used for the calculations.

We assume that the transversely isotropic stress-strain relations (Equation (1)) are appropriate for the Aztec Sandstone with well developed cross-beds as

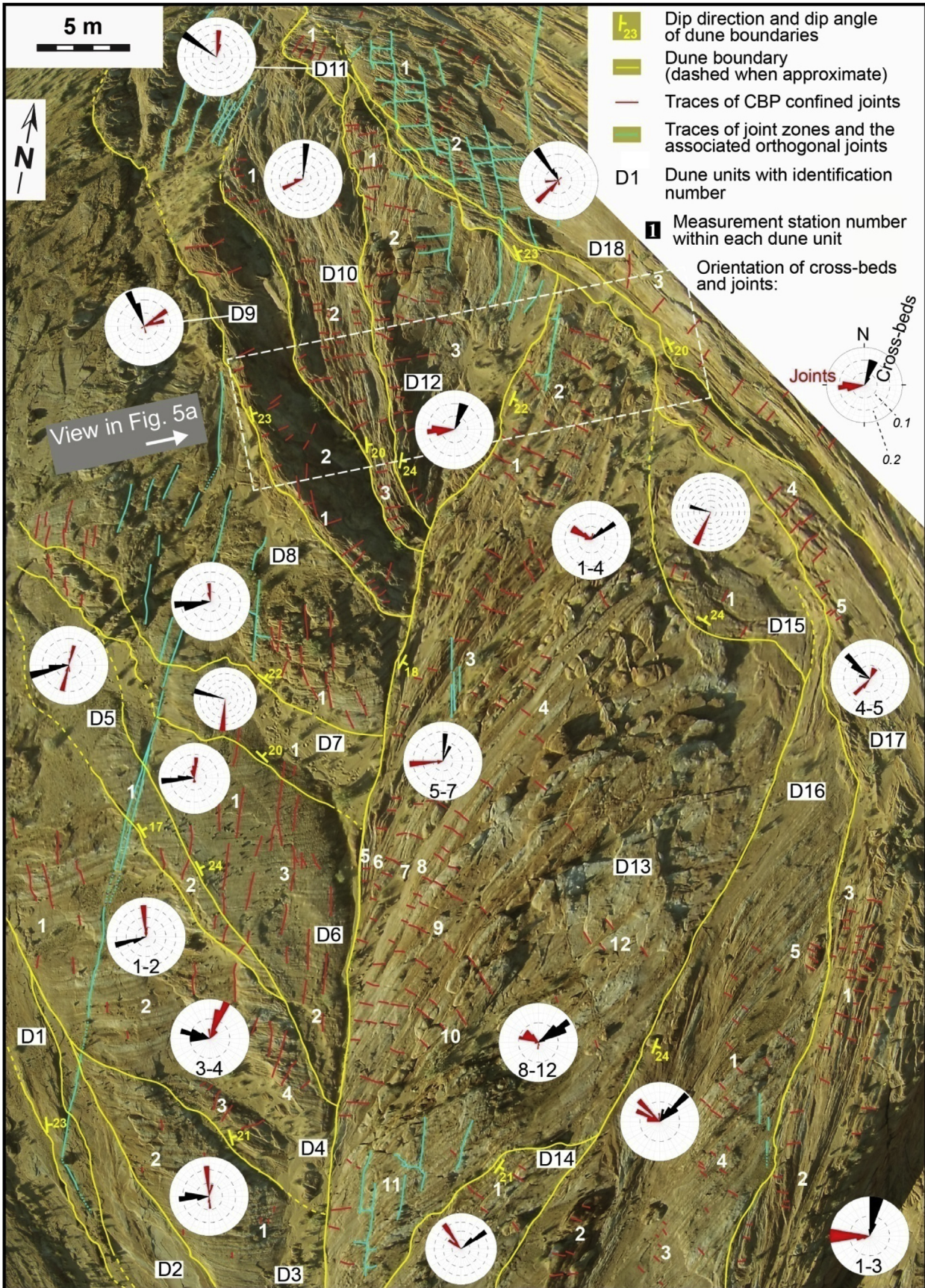


Fig. 3. Map of the main study area (location “A” in Fig. 1) on a mosaic of low altitude aerial photographs taken from an unmanned aerial vehicle. The map shows dunes that are numbered for identification purposes and various sets of joints traces (in red). Rose diagrams showing the measured strikes of cross-beds (in black) and joints (in red) are used for

$$\begin{bmatrix} \varepsilon_{11} \\ \varepsilon_{22} \\ \varepsilon_{33} \\ 2\varepsilon_{23} \\ 2\varepsilon_{13} \\ 2\varepsilon_{12} \end{bmatrix} = \begin{bmatrix} \frac{1}{E} & -\frac{\nu}{E} & -\frac{\nu'}{E} & 0 & 0 & 0 \\ & \frac{1}{E} & -\frac{\nu'}{E} & 0 & 0 & 0 \\ & & \frac{1}{E'} & 0 & 0 & 0 \\ & \dots & & \frac{1}{G} & 0 & 0 \\ & & & & \frac{1}{G} & 0 \\ & & & & & \frac{1}{G} \end{bmatrix} \begin{bmatrix} \sigma_{11} \\ \sigma_{22} \\ \sigma_{33} \\ \sigma_{23} \\ \sigma_{13} \\ \sigma_{12} \end{bmatrix} \quad (1)$$

$$G = \frac{2(1+\nu)}{E}$$

where plane 1–2 is the plane of isotropy (bedding plane) and axis 3 is of rotational symmetry (Lekhnitskii, 1963). Five independent elastic moduli ( $E$ ,  $\nu$ ,  $E'$ ,  $\nu'$  and  $G$ ) are in the symmetric compliance matrix  $S$ .  $E$  and  $\nu$  are Young's modulus and Poisson's ratio for an applied normal stress in the plane of isotropy.  $E'$  and  $\nu'$  are Young's modulus and Poisson's ratio for an applied normal stress perpendicular to the plane of isotropy.  $G$  is the shear modulus corresponding to the shear stress applied in planes perpendicular to the plane of transverse isotropy. In this paper, we use the convention that tensile stresses and tensile strains are positive.

In a general triaxial test run, the sample was first jacketed in shrink tubing to aid assembly, followed by polyurethane tubing that was clamped to steel end plugs. The sample assembly was then placed in a pressure vessel in a triaxial loading apparatus similar to the test configuration described in Lockner and Stanchits (2002). Samples were evacuated for approximately 30 min and then saturated with deionized water for all tests. The tests were conducted at ambient confining pressures ranging from 10 to 40 MPa and deviatoric stress from 0 to 40 MPa. Pore pressure was held constant at 10 MPa. Pore volume change ( $\Delta V_{pore}$ ) in response to axial and confining pressure changes was recorded. During the test, a piston pushes against the end of the sample to produce axial stress  $\sigma_a$ , while pressurized fluid (oil) produced lateral confinement,  $P_c$ . Two cycles of axial stress changes were made at each confining pressure level to reduce the effect of time-dependent creep on the measurement of elastic properties. Elastic moduli were measured during the unloading step of the second cycle.

In this axisymmetric configuration (Fig. 2b),  $\sigma_{11} = \sigma_{22} = P_c$  and  $\sigma_{33} = \sigma_a$ . According to equation (1), changes in axial stress ( $\sigma_a$ ) and axial strain ( $\varepsilon_a$ ) will give:

$$E' = \frac{\Delta\sigma_{33}}{\Delta\varepsilon_{33}} = \frac{\Delta\sigma_a}{\Delta\varepsilon_a} \quad (2)$$

and

$$\nu' = -\frac{\Delta\varepsilon_{11}}{\Delta\varepsilon_{33}} = -\frac{\Delta\varepsilon_{vol} - \Delta\varepsilon_a}{2\Delta\varepsilon_a} \quad (3)$$

Assuming the volume change of the matrix ( $\Delta V_{matrix}$ ) is substantially smaller than the pore volume change ( $\Delta V_{pore}$ ):

$$\Delta V_{sample} = \Delta V_{pore} + \Delta V_{matrix} \approx \Delta V_{pore} \quad (4)$$

Volumetric strain can then be calculated by

$$\Delta\varepsilon_{vol} = \frac{\Delta V_{sample}}{V_{sample}} \approx \frac{\Delta V_{pore}}{V_{sample}} \quad (5)$$

Independent calibration runs measuring Young's modulus were performed using an aluminum sample and three Berea Sandstone samples. The measurements of Young's modulus demand that the sample end faces be parallel within 0.2 mm, constraining measurement error to about 2%. Initially, samples A, B and C were designed for measuring  $E$ ,  $\nu$ ,  $E'$ ,  $\nu'$  using a triaxial test for determining the stiffness anisotropy. However, we found that difficulties in maintaining precise sample dimensions especially for bedding-parallel samples, exacerbated by the intrinsic sample heterogeneity prevented reliable determinations of  $E$ , and  $\nu$  particularly from samples "B" and "C". Consequently, only samples of "A" configuration (Fig. 2b) of selected sets (1A, 3A and 4A) are used for measuring  $E'$ ,  $\nu'$ . Velocity measurements were conducted on samples of "B" and "C" configuration for determining the P-wave (by extension, elastic modulus) anisotropy.

The P-wave velocity measurements were made at ambient pressure and temperature conditions. The bench-top ultrasonic assembly consisted of a pair of P-wave transducers (from Olympus Panametrics with 1 MHz central frequency), an oscilloscope (Tektronix TDS 3014C) and a pulse generator. Transducer delay time was determined by placing the transducers in contact with each other (head-to-head). The travel time for P-waves through the sample was then determined by positioning the sample at a fixed position with a load of about 1.3 kg to ensure consistent coupling for each measurement. Time of P wave arrival was determined by manually picking the first peak after correcting for transducer delay time. Velocity was calculated by dividing the sample length with the arrival time. The measurements were confirmed with standard aluminum samples.

P-wave velocities were measured parallel ( $V_{p11}$ ) and perpendicular to bedding ( $V_{p33}$ ) on 11 samples of the Aztec Sandstone cut in "B" and "C" configurations (Fig. 2a and c) to determine the P-wave anisotropy ( $\varepsilon_p$ ) as:

$$\varepsilon_p \approx \frac{V_{p11} - V_{p33}}{V_{p33}} \quad (6)$$

To follow the convention in rock physics (Thomsen, 1986; Mavko et al., 2009, p37),  $\varepsilon$  is used with a subscript "p" here, which distinguishes this parameter from  $\varepsilon_{ij}$  for the strain components. In addition, P-wave velocities were also measured in two orthogonal directions parallel to bedding ( $V_{p11}$  and  $V_{p22}$ ) on five samples of "A" configuration. (Fig. 2d).

## 4. Field data

### 4.1. Depositional architecture

The aeolian deposits in the study area (Site A) consist of a number of dune units with predominantly NNW-NNE oriented dune boundaries with dip angles generally less than 30° (Figs. 3 and 4). According to the truncating relationship between these

visual and numerical comparison about the changes in cross-bed orientation and joint orientations at 49 measurement stations from different dunes. In the rose diagrams, every bin represents the strike interval of 10°. The length of each bin reflects the percentage of the total measurements (about 24 on average). Every black dashed circle represents 10 percent of the measurements at the stations cumulatively (see the inset). Notice that the cross-beds are characterized by the hues of orange and white stripes on the photograph. The location of Fig. 5a is labeled with a dashed white line rectangle.

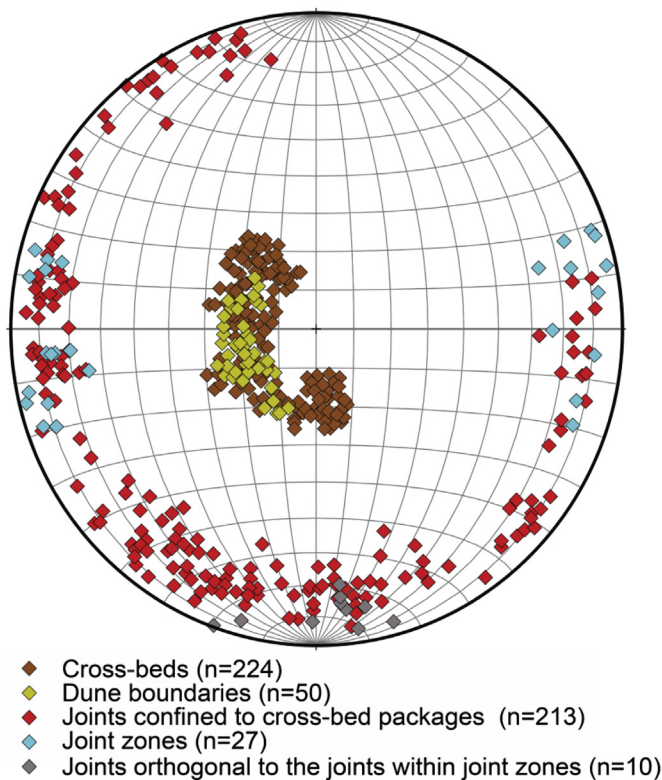


Fig. 4. Attitudes (poles to planes, equal area stereonet and lower hemisphere projection) of cross-beds, dune boundaries, and three sets of joints measured in the field area.

bounding surfaces, 18 dune units were identified and named from older to younger (D1–D18) within the mapping area. The sequential relationship between certain dunes, such as D14 and D15, is difficult to determine because of the lack of geomorphic contact. Compared to the dune boundaries, the orientation of cross-beds have a much broader distribution of strikes ranging from  $0^\circ$  to  $70^\circ$  and  $188^\circ$  to  $355^\circ$  (Fig. 4). Dip angles of cross-beds vary between  $12^\circ$  and  $30^\circ$  with a mean of  $21^\circ$ .

Morphologic, depositional, and structural resemblances and differences among these 18 dune units confined mostly by second-order dune boundaries were checked by visual inspection and numerous field measurements of cross-bed orientations. The number of stations (MS) selected for orientation measurements in a unit, depended on the variability of the cross-bed orientations within a dune (Fig. 3). These are shown by rose diagrams in Fig. 3. For example, in the northern part of dune D4, the nearly WSW-striking cross-beds (black in the rose diagram for MS 1–2 in the figure) change to about WNW-striking cross-beds in the southern part (MS 3–4). While clearly visible in the rose diagrams, the differences in cross-bed orientations are also reflected by the trends of white–orange stripes in the background mosaic photographs (Fig. 3). A larger degree of change in cross-bed orientations within a single dune was also observed, for instance, in D13 and D17 (see rose diagrams MS 1–4 and MS 5–7 in D13; MS 1–3 and MS 4–5 in D17 in Fig. 3).

In addition to the variation of cross-bed orientations within a single dune, differences between the orientations of cross-beds from one dune to the next can also be significant. For instance, the cross-beds in D3, D6, D7, and D8 are roughly W-striking, whereas the cross-beds in D13 immediately adjacent to this boundary are nearly N-striking. Similar changes can also be observed from D8, D10, D12, and D16 to D9, D11, D13 (MS1–4), and D17, respectively.

## 4.2. Joint sets

Based on the orientation, geometry, and relationship with cross-beds and dune boundaries, we identified three distinct joint sets across the mapping area: (1) Cross-bed package confined joints; (2) joint zones that are approximately north-south trending and relatively continuous; and (3) joints orthogonal to the members of joint zones.

### 4.2.1. Cross-bed package confined joints

Cross-bed package confined joints occur within a bundle of cross-beds, but are bounded by the cross-bedding interfaces at the package boundaries. The concept of cross-bed package (CBP) is equivalent to that of a mechanical layer (Narr, 1991; Gross, 1995; Cooke et al., 2006; Laubach et al., 2009), which lies between bed-parallel surfaces. From here on, joints confined within CBP and terminate at the package boundaries will be referred to as CBP joints for brevity. The orientations of CBP joints are characterized by a broad distribution of strikes ranging from  $0^\circ$  to  $80^\circ$  and from  $170^\circ$  to  $356^\circ$ . Dip angles of the CBP joints vary between  $58^\circ$  and  $89^\circ$  with a mean value of  $76^\circ$  (Fig. 4), but they occur at high-angle to cross-bedding (Fig. 5). To better understand the relationships between cross-beds and the CBP joints, trace geometries of these joints on erosional surfaces (pavements and scarps) were mapped in the study area (Fig. 3). The orientations of CBP joints as well as the orientations of cross-beds in which they occur were measured at 49 stations. The data are plotted in Figs. 3–7. These figures show several systematic features:

- 1) In the rose diagrams in Fig. 3, the joints (red bins) and the cross-beds (black bins) are approximately orthogonal to each other. Such a pattern in the strikes of cross-beds and CBP joints remains more or less consistent as the cross-bed orientations vary widely. For example, corresponding to the transition from WSW-striking cross-beds in the northern part of dune, D4 (MS 1–2), to nearly WNW-striking cross-beds in the southern part (MS 3–4), the CBP joints change from NNW-striking to NNE-striking. Significant variations of strikes of CBP joints within a single dune unit are also observed. For example, in the northern part of D13 (MS 1–4), the cross-beds have NE-strikes and the CBP joints therein have NW-strikes. Following the change of cross-beds to a northerly strike in the western part of the same dune (MS 5–7), the CBP joints also change to a western strike maintaining a sub-perpendicular relationship. Aside from the variation in CBP confined joint orientations within a dune, significant differences are also observed between the orientations of CBP confined joints in two adjacent dune units. The CBP joints in D3, D6, D7 and D8 adjacent to the lower boundary of D13 have approximately N–S strikes. In comparison, the CBP joints change to a W-strike on D13 (MS 5–7). Contrasting differences in the orientations of CBP joints can also be observed from D8, D10, D12, and D16 to D9, D11, D13 (MS 1–4), and D17, respectively.
- 2) The orientation data can be plotted to highlight trends in the mean values of the measured strikes of the joints as a function of the cross-beds (Fig. 6). The plot shows two roughly sub-parallel trends of strikes of cross-beds (black) and of CBP joints (grey) over all measurement stations. Notice that the outliers (MS 1 in D5, MS 2 in D9 and MS 3 in D18) are due to certain high-angle joints dipping to the opposite direction, resulting in a nearly  $180^\circ$  difference (right-hand-rule convention) in strike values of the same joint set. The dip angle of cross-beds (from  $12^\circ$  to  $30^\circ$ ) and CBP joints (from  $58^\circ$  to  $89^\circ$ ) have relatively smaller variations as can be seen in Fig. 4 and therefore are not shown here.

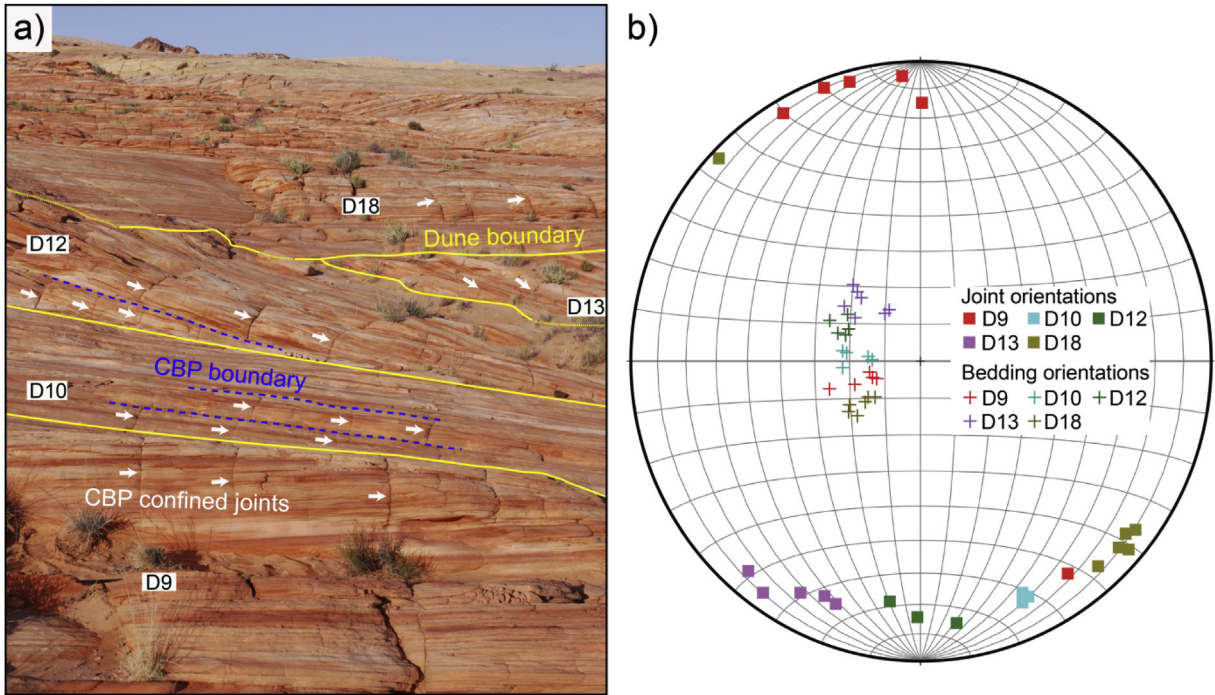


**Fig. 5.** Dune units (D9, D10, D12, D13 and D18) with contrastingly different cross-bed orientations and the variation of cross-bed package joints orientations. a). Ground photograph including multiple dune units in which dune boundaries (yellow lines), some cross-bed package boundaries (blue dashed lines), and joints (indicated by white arrows) are labeled. For the location of the photograph, see Fig. 3 b). Stereonet (poles to planes, equal area stereonet and lower hemisphere projection) showing the variation of cross-bed orientations across the dune units and the variation of joint orientations therein (45 data points).

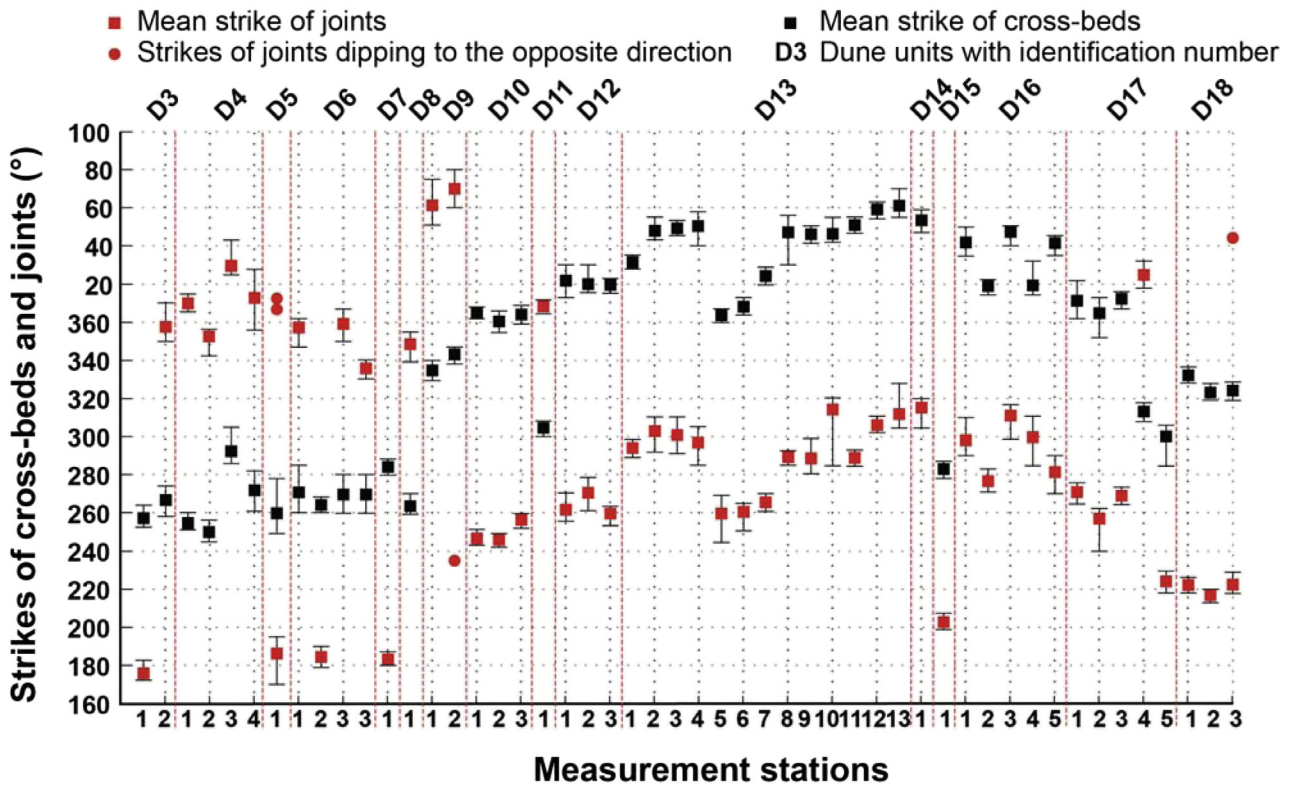


**Fig. 6.** Plot showing the mean values and the range of measured strikes of cross-beds (black) and cross-bed package confined joints (grey) at each measurement station.

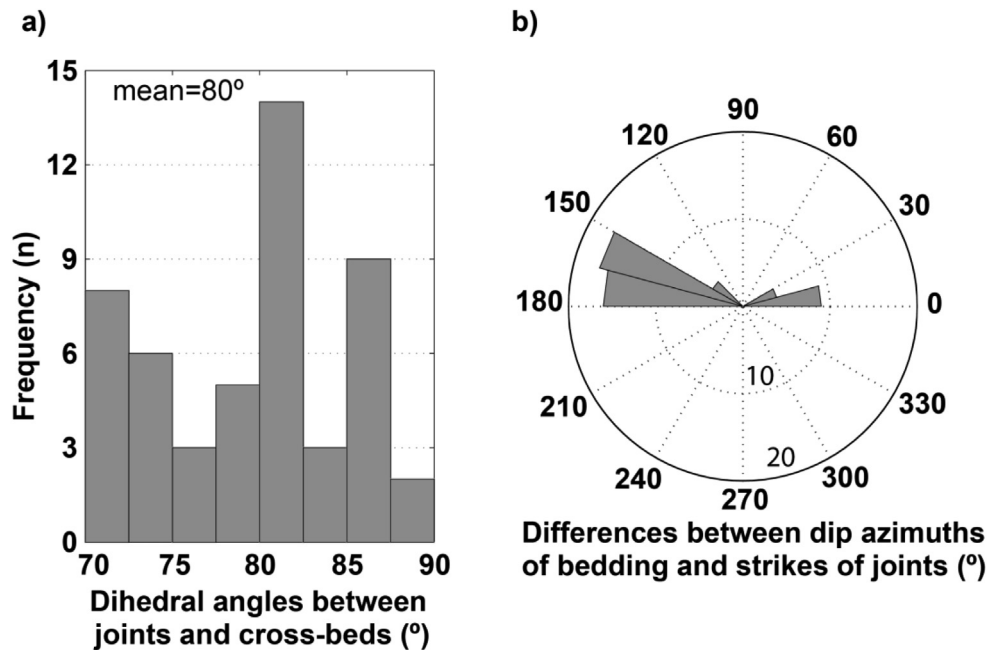


**Fig. 7.** Distribution plots of dihedral angles (a) and azimuth differences (b) between cross-beds and cross-bed package confined joints. In (b) each bin represents a strike interval of 15°. The length of each bin reflects the number of measurements (“10” and “20” labeled at each circle).

3) Using the mean values of orientations calculated from the data collected from each measurement station, the dihedral angles between the cross-beds and CBP joints and the difference between the dip azimuths of bedding and strike azimuths of CBP joints can be determined (Fig. 7). In general, the dihedral angles between the CBP joints and cross-beds range from 70° to 88° with the mean value of about 80° and a standard deviation of about 6°. (Fig. 7a). The differences between the dip azimuths of bedding and strike azimuths of CBP joints vary from 0° to 26° and more frequently from 147° to 177° (Fig. 7b). These results suggest that (1) CBP joints are at high-angle to bedding but not strictly perpendicular to bedding everywhere, and that (2) CBP joints trend roughly parallel to the dip direction of the cross-beds.

#### 4.2.2. Joint zones and the associated orthogonal joints

Joint zones in the mapping area are clusters of sub-parallel joints with strikes ranging from 355° to 15° and from 161° to 200° (Figs. 4 and 8). Dip angles of these zonal joints vary between 64° and 88°. Based on the abutting relationships, joint zones appear to be older than CBP joints in a few places (For instance, MS 3 in D3 in Fig. 3; middle right part of Fig. 8) and are more continuous across the dunes. Many joint zones occur as through-going features in cross-beds of various orientations and have relatively similar orientations. A good example of this can be found in the western part of the map (Fig. 3), where a joint zone occurs as a continuous feature through D1 to D8. Although the joint zones appear to be not significantly influenced by the variation of cross-bed orientation, some joint zones are truncated by certain dune boundaries. For instance, the aforementioned joint zone ends adjacent to the lower boundary of D1 and conjoins with a segment parallel to that dune boundary. Similarly, segments of the joint zone in the northern part of D18 are bounded by the lower dune boundary of D18. Besides the joint zones that are continuous across cross-beds of various orientations, less continuous joint zones are present. They occur in the northern part (MS 2), western part (MS 3), and southern part (MS 11) of dune D13 and eastern part of D16 (MS 4) (Fig. 3).

Similar to the nearly N–S trending joint zones mapped by Taylor et al. (1999) and Myers and Aydin (2004), the joint zones documented in this study have complicated internal architectures (Fig. 8). Certain parts of these zones might be splay fractures emanating from shearing of pre-existing joints, joint zones or bedding interfaces (Myers and Aydin, 2004). The complete characterization of these joint zones requires detailed mapping and more data collection. However, because the focus of this study is the orientation of joint sets and their relationship with cross-bed orientations, the characteristics (e.g., segments and internal architectures) of the joint zones are only briefly described here. Interested readers are referred to Meyers and Aydin (2004); Flodin and Aydin (2004); and de Jossineau and Aydin (2007) for small faults formed by shearing of joint zones of various geometry.

**Joints orthogonal to the joints within joint zones** are systematically confined or truncated against the through-going joints of the joint zones (Figs. 4 and 8). Based on this truncation relationship, this joint set is younger than the joint zones and has an origin consistent with the orthogonal jointing concept (e.g., Bai et al. (2002)).

## 5. Static moduli and P-wave anisotropy

### 5.1. Static moduli

The measured elastic modulus  $E'$  ranges from 4.8 GPa to 6.5 GPa for all three samples (Fig. 9).  $E'$  also increases as a function of effective confining pressure. Sample 3A has relatively higher  $E'$  (from 5.1 GPa to 6.5 GPa) whereas sample 1A has relatively lower  $E'$  (from 4.8 GPa to 5.8 GPa). All three samples show an almost linear trend of  $E'$  with the increase of confining pressure (Fig. 9). Poisson's ratio  $\nu$  measured at confining pressure of 20 MPa are 0.36, 0.35 and 0.37 for samples 1A, 3A and 4A, respectively. The errors of the measurements of Young's modulus  $E'$  and Poisson's ratio  $\nu$  are mainly related to the uncertainty in sample dimension ( $\pm 1.5\%$ ), uncertainty in the machine calibration ( $\pm 2\%$ ) and in the piston correction ( $\pm 3\%$ ). An estimate of the overall error is about  $\pm 4\%$  for each sample. Relative changes in modulus as a function of confining

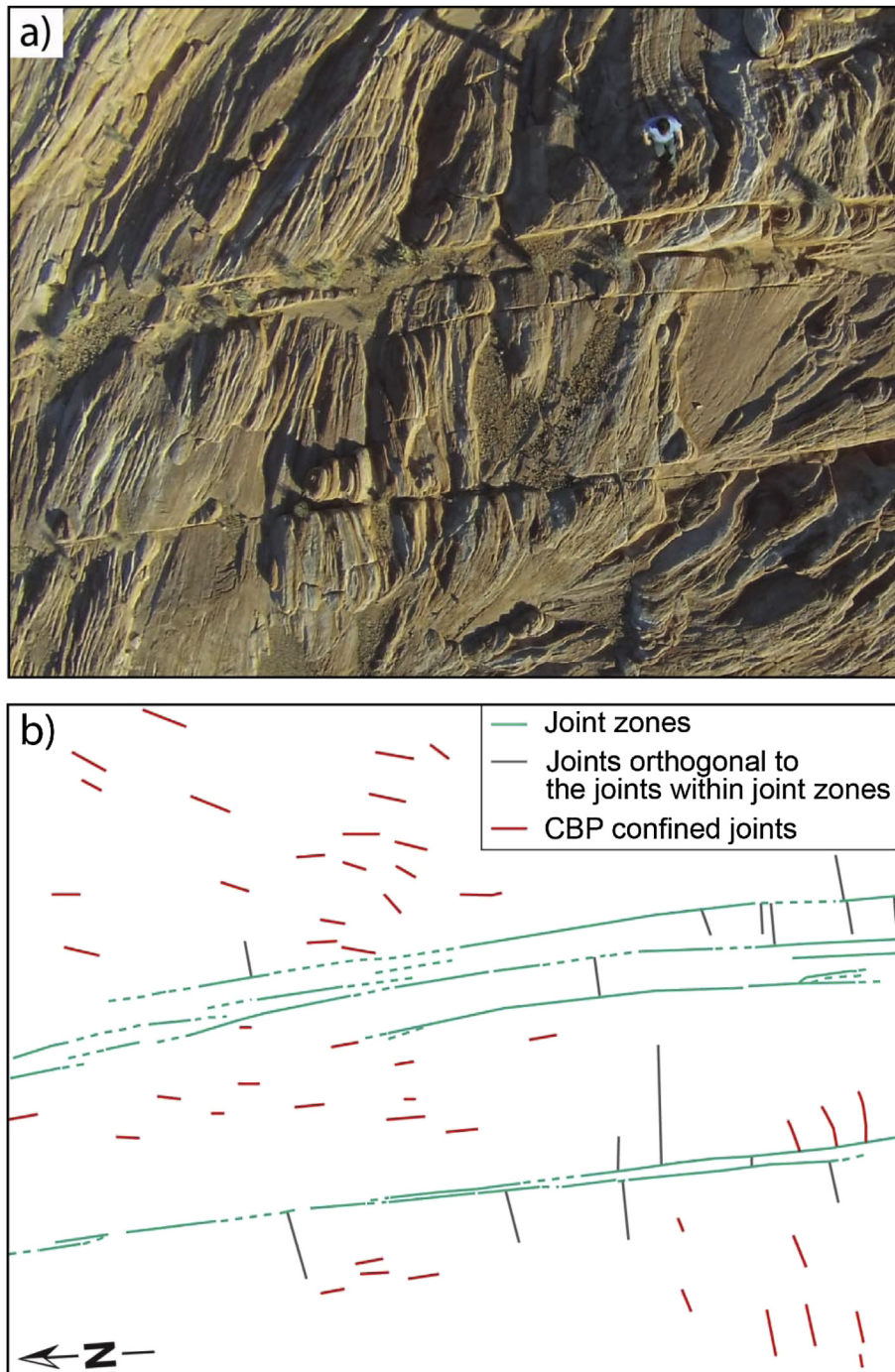


**Fig. 8.** a). Field photograph taken by unmanned aerial vehicle in the northern part of dune D9 (man for scale). b). Schematic drawing of joint sets in (a) showing joint zones and their internal architecture (dashed when approximate), joints orthogonal to those within joint zones, and cross-bed package (CBP) joints. Notice that several CBP joints are truncated against a member of the joint zones in the middle right part of the figure. There are cross-bed domains of different orientations in the lower part and at least one member of the joint zones occurs as through-going features therein.

pressure for an individual sample are better determined (less than  $\pm 0.5\%$ ) because uncertainties in sample dimensions and machine stiffness corrections cancel.

## 5.2. P-wave anisotropy

P-wave velocities along different directions with respect to bedding were measured from 16 samples. Accuracy of P-wave determinations were limited by the uncertainty in sample dimension

( $\pm 1.5\%$ ) and the  $\pm 1 \mu s$  difference in the travel time caused by variations in sample alignment as determined by repeat measurements. Estimated overall uncertainty in P-wave velocity measurements is about  $\pm 5\%$  for each sample. The measured data as well as P-wave anisotropies of different values show several systematic features (Fig. 10).

1) The measured P-wave anisotropy  $\epsilon_p$  (Equation (6)) ranges from  $-5\%$  (sample 2C) to  $36\%$  (sample 6C). Positive P-wave

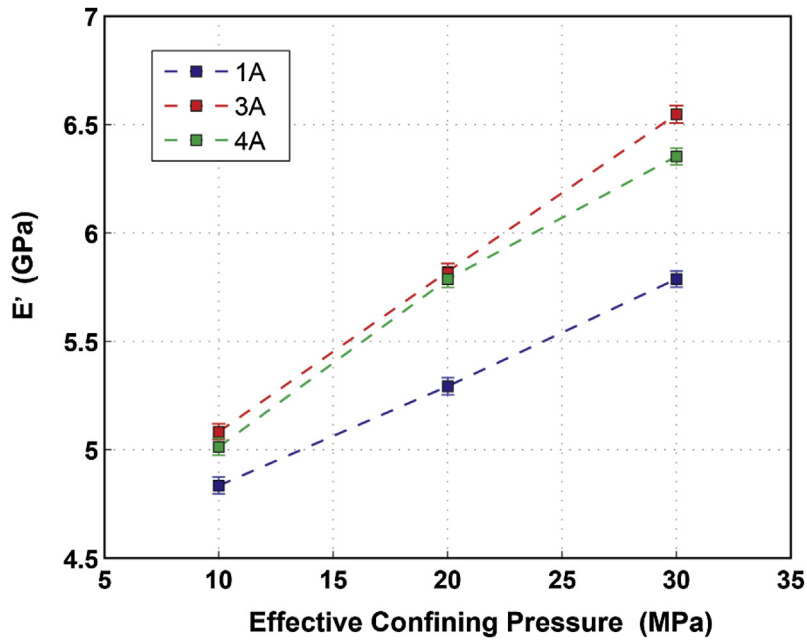


Fig. 9. Plot showing measured Young's modulus ( $E$ ) of samples 1A, 3A and 4A at different effective confining pressures (10, 20 and 30 MPa). The trends of each data set were highlighted by the dashed lines connecting the data points.

anisotropy ( $V_{p11} > V_{p33}$ , the "3" direction is perpendicular to bedding) are found for all measured samples except sample 2C ( $V_{p11} < V_{p33}$ ). A majority (8 out of 11) of the data set have measured  $\epsilon$  varying between 5% and 20% (Fig. 10a). Though the degree of anisotropy varies from sample to sample, an average P-wave anisotropy for all 11 measured samples is 13.3%.

2) P-wave velocities parallel to bedding but in two orthogonal directions (Fig. 2d) were measured from 5 samples (Fig. 10b). The differences between measured values of  $V_{p11}$  and  $V_{p22}$  roughly

vary between  $\pm 5\%$ . This variation is relatively smaller than the average P-wave anisotropy (13.3%).

3) The P-wave velocities measured from individual samples (A, B and C) and different sample sets (Set 1–6) range widely from 1.05 km/s ( $V_{p11}$  of sample 2C) to 2.23 km/s ( $V_{p11}$  of sample 3A). Significant differences exist not only among different sample sets (for instance, Set 3 and Set 6), but also among each set of three samples (for instance,  $V_{p11}$  measured from 1A, 1B and 1C).

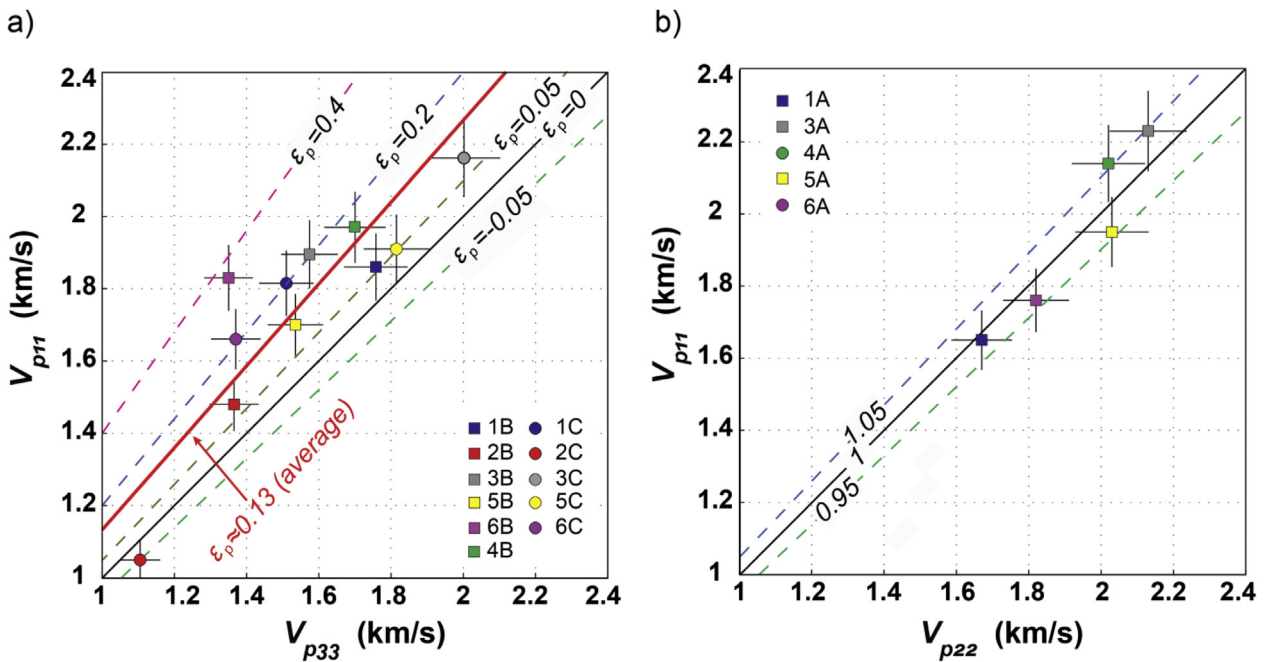


Fig. 10. Measured P-wave velocities along different directions with respect to cross-bedding. a). Comparison of measured  $V_{p11}$  with  $V_{p33}$  from 11 samples of "B" and "C" configuration. P-wave anisotropies  $\epsilon_p$  (Equation (6)) of different values are shown by dashed lines denoted by colors and numbers ( $-0.05, 0, 0.05, 0.2, 0.4$ ). b). Comparison of measured  $V_{p11}$  with  $V_{p22}$  from 5 samples of "A" configuration. Different values of  $V_{p11}/V_{p22}$  are shown by lines denoted by colors and numbers (0.95, 1, 1.05). In both a) and b), the errors of the measurements ( $\pm 5\%$ ) are given by the horizontal and vertical bars.

## 6. Effects of anisotropy on principal stress orientation

### 6.1. Model configuration and boundary conditions

The average P-wave anisotropy reported in Section 5.2 suggests that the cross-bedded Aztec Sandstone is elastically anisotropic. To understand how the cross-bedding associated anisotropy affects the formation and orientation of joints in aeolian Aztec Sandstone, a model based on the generalized Hooke's law for anisotropic materials (Lekhnitskii, 1963) is analyzed assuming that the cross-bedded sandstone is transversely isotropic (Equation (1)).

The model geometry and the applied boundary conditions are shown in Fig. 11a. The infinite transversely isotropic medium representing the cross-bedded sandstones is subjected to strain boundary conditions (BC). The principal strain components ( $\epsilon_1$ ,  $\epsilon_2$  and  $\epsilon_3$  are coaxial with x-, y- and z-axis, Fig. 11a) and material properties (MP) ( $E$ ,  $\nu$ ,  $E'$ ,  $\nu'$  and  $G'$  in Equation (1)) are used to investigate the effect of elastic anisotropy on the orientation and magnitude of the maximum principal stress component ( $\sigma_1$ ) (Fig. 11b), which is of interest for jointing. The strain boundary conditions, material properties and stress components are related by Equation (7) which follows from Equation (1).

$$\begin{pmatrix} \sigma_{xx} \\ \sigma_{yy} \\ \sigma_{zz} \\ \sigma_{yz} \\ \sigma_{xz} \\ \sigma_{xy} \end{pmatrix} = [S'(\alpha_1, \theta_1, S)]^{-1} \begin{pmatrix} \epsilon_{xx} \\ \epsilon_{yy} \\ \epsilon_{zz} \\ 0 \\ 0 \\ 0 \end{pmatrix} \quad (7)$$

where  $S'$  (six by six compliance matrix) is a function of  $\alpha_1$ ,  $\theta_1$  and  $S$ . The transformed compliance matrix ( $S'$ ) of cross-beds of different orientations ( $\alpha_1$ ,  $\theta_1$ ) in the (x, y, z) cartesian coordinate system is obtained by operating coordinate transformations on  $S$  (Mavko et al., 2009, p. 20). The magnitude and orientation of the maximum principal stress component ( $\sigma_1$ ) is determined by solving the eigenvalue problem (e.g. Pollard and Fletcher, 2005, p. 219) of the stress tensor written in the column vector form in Equation (7).

In the analysis, the strike orientation ( $\alpha_1$ ) of cross-beds (Fig. 11a) varies from  $0^\circ$  to  $359^\circ$ . The dip angle ( $\theta_1$ ) of cross-beds is kept constant at  $21^\circ$  for simplicity based on the average dip angle of the cross-beds observed in the field. For the material

properties (MP), we use representative values (for instance,  $E = E' = 5$  GPa,  $\nu = \nu' = 0.35$  for the isotropic case) for the elastic moduli ( $E$ ,  $\nu$ ,  $E'$ ,  $\nu'$  and  $G'$ ) based on the results from the static measurements reported (Section 5.1). According to the measured average P-wave anisotropy ( $V_{p11} > V_{p33}$ ), we assume that  $E$  is larger than  $E'$  for all anisotropic cases.

### 6.2. Model results

Five different material properties (MP1-MP5) in combination with four different remote strain boundary conditions (BC1-BC4) were investigated in a total of eight cases (Case 1 to Case 8). Similar to the commonly applied strain boundary conditions in extension testing (i.e. Rutter, 1998), these four strain boundary conditions are uniaxial extension (BC1:  $\epsilon_{zz} > \epsilon_{xx} = \epsilon_{yy} = 0$ ), axisymmetric extensions (BC2:  $\epsilon_{zz} > \epsilon_{xx} = \epsilon_{yy}$ ; BC3:  $\epsilon_{zz} < \epsilon_{xx} = \epsilon_{yy}$ ) and triaxial extension (BC4:  $\epsilon_{xx} > \epsilon_{yy} > \epsilon_{zz}$ ). The details about the model results are presented in Fig. 12 and summarized in Table 1.

The results summarized in Table 1 suggest that the interplay between the anisotropy of a medium and the applied strains results in different principal stress orientations, i.e., the plunge directions and plunge of  $\sigma_1$  (the maximum principal tension).

While Case 1 (the only case with isotropic medium) shows no variation and Case 5 (the only case with triaxial extension) shows relatively small variation, all other cases show significant changes of  $\sigma_1$  plunge directions as the strikes of cross-beds vary (Fig. 12a, Table 1). Particularly, in Cases 2 and 3, the difference between the plunge direction ( $\alpha_2$ ) of  $\sigma_1$  and the strike of cross-beds ( $\alpha_1$ ) is constant as  $90^\circ$  as the latter varies. However, in Cases 4, 6, 7 and 8, the plunge direction ( $\alpha_2$ ) of  $\sigma_1$  and the strike of cross-beds ( $\alpha_1$ ) are the same as the latter varies.

Although Case 3 ( $\epsilon_{zz} > \epsilon_{xx} = \epsilon_{yy}$ ) and Cases 4, 6, 7 and 8 ( $\epsilon_{zz} < \epsilon_{xx} = \epsilon_{yy}$ ) all have axisymmetric extension as the boundary conditions, the difference in the relative magnitudes between  $\epsilon_{zz}$  and  $\epsilon_{xx}(\epsilon_{yy})$  here results in different variations of  $\alpha_2$  with respect to  $\alpha_1$ .

Regarding the plunge of  $\sigma_1$ , Case 5 shows a certain degree of variation whereas other cases have different but constant values with respect to strikes of cross-beds (Fig. 12b, Table 1). In particular, Cases 2 ( $\epsilon_{zz} > \epsilon_{xx} = \epsilon_{yy} = 0$ ) and 3 ( $\epsilon_{zz} > \epsilon_{xx} = \epsilon_{yy} \neq 0$ ) have different plunges of  $\sigma_1$  due to distinct applied boundary conditions, though these two cases are characterized by the same variation of the plunge direction of  $\sigma_1$  as mentioned above. In

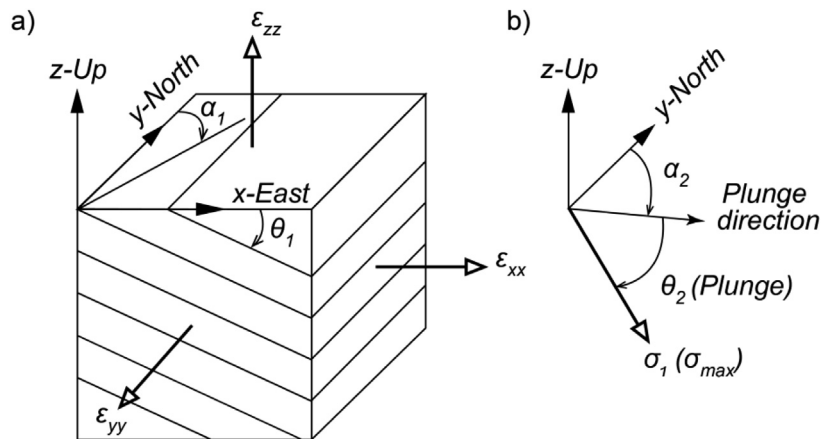


**Fig. 11.** Illustration of the model configuration: cross-bed orientation, three dimensional strain, plunge direction and plunge (Pollard and Fletcher, 2005) of the maximum principal stress component. a). Schematic diagram showing cross-bed strike  $\alpha_1$  and dip angle  $\theta_1$  and three principal strain components ( $\epsilon_{xx}$ ,  $\epsilon_{yy}$  and  $\epsilon_{zz}$ ) applied as boundary conditions. The (x, y, z) Cartesian coordinate system for the strain components is consistent with the (east, north, up) ENU coordinate system in which the cross-bed orientation is defined. b). Diagram showing plunge direction ( $\alpha_2$ ) and plunge ( $\theta_2$ ) of the maximum principal stress component ( $\sigma_1$ ).

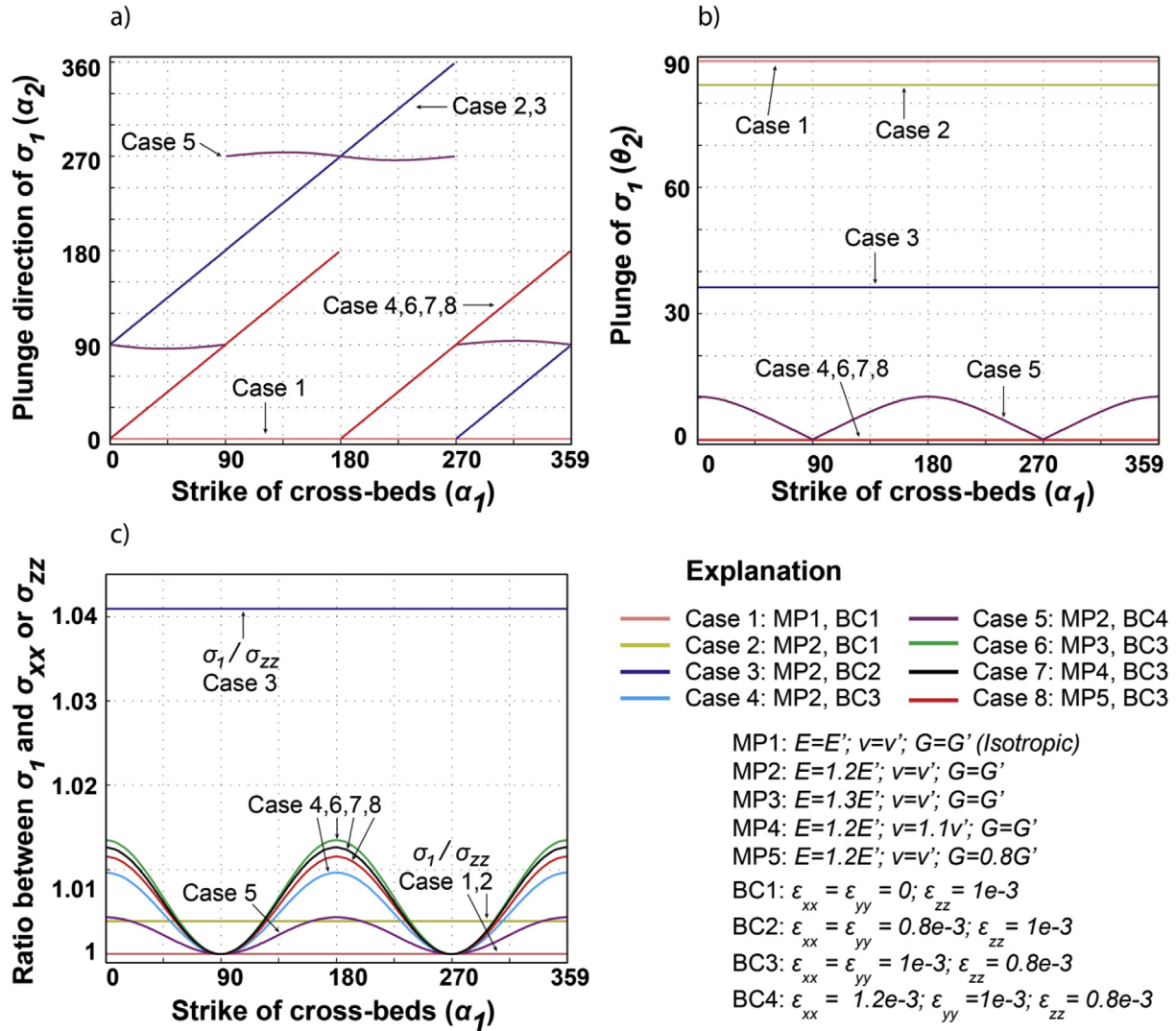


**Fig. 12.** Model results for Case 1 to Case 8 (see the explanation). a) Plunge direction ( $\alpha_2$ ) of maximum principal stress component ( $\sigma_1$ ) for cross-beds of various strike orientations ( $\alpha_1$ ). b) plunge ( $\theta_2$ ) of  $\sigma_1$  in cross-beds of various  $\alpha_1$ . c) Ratio between the magnitudes of  $\sigma_1$  and  $\sigma_{xx}$  or  $\sigma_{zz}$ . For the cases, Case 1 to Case 3, in which  $\epsilon_{zz}$  is the maximum strain component,  $\sigma_1/\sigma_{zz}$  is plotted. For Case 4 to Case 8, in which  $\epsilon_{xx}$  is the maximum strain component,  $\sigma_1/\sigma_{xx}$  is plotted.

comparison, Cases 4, 6, 7 and 8 have the same value for the plunge of  $\sigma_1$  because of the identical applied boundary condition ( $\epsilon_{zz} < \epsilon_{xx} = \epsilon_{yy}$ ). The differences between Cases 4, 6, 7 and 8 are the distinct ratios between  $\sigma_1$  and  $\sigma_{xx}$  (Fig. 12c) due to different

material properties. For instance, as the degree of stiffness anisotropy becomes greater from MP2 ( $E=1.2E'$ ) to MP3 ( $E=1.3E'$ ), the maximum ratio between  $\sigma_1$  and  $\sigma_{xx}$  increases slightly from 1.01 (Case 4) to 1.013 (Case 6).

**Table 1**  
Summary of the model results presented in Fig. 12.

Cases	Material properties	Boundary conditions	$\sigma_1$ plunge directions ( $\alpha_2$ )	$\sigma_1$ plunge ( $\theta_2$ )	Ratios between $\sigma_1$ and $\sigma_{zz}$ or $\sigma_{xx}$
Case 1	MP1: Isotropic medium	BC1: uniaxial extension ( $\epsilon_{zz} > \epsilon_{xx} = \epsilon_{yy} = 0$ )	0°	90°	1; coaxial with $\epsilon_1$ ( $\epsilon_{zz}$ )
Case 2	MP2: Anisotropic medium ( $E=1.2E'$ )	BC1: uniaxial extension ( $\epsilon_{zz} > \epsilon_{xx} = \epsilon_{yy} = 0$ )	Difference between $\alpha_2$ and $\alpha_1$ is constant as 90°	84.3°	~1.005; not coaxial with $\epsilon_1$ ( $\epsilon_{zz}$ )
Case 3	MP2: Anisotropic medium ( $E=1.2E'$ )	BC2: axisymmetric extension ( $\epsilon_{zz} > \epsilon_{xx} = \epsilon_{yy}$ )	Difference between $\alpha_2$ and $\alpha_1$ is constant as 90°	36.1°	~1.04; not coaxial with $\epsilon_1$ ( $\epsilon_{zz}$ )
Case 4	MP2: Anisotropic medium ( $E=1.2E'$ )	BC3: axisymmetric extension ( $\epsilon_{zz} < \epsilon_{xx} = \epsilon_{yy}$ )	$\alpha_2$ is equal to $\alpha_1$ or 180°	0°	Varies between 1 and 1.01; mostly not coaxial with $\epsilon_1$ ( $\epsilon_{xx}, \epsilon_{yy}$ )
Case 5	MP2: Anisotropic medium ( $E=1.2E'$ )	BC4: triaxial extension ( $\epsilon_{xx} > \epsilon_{yy} > \epsilon_{zz}$ )	Varies around 90° ± 4° and 270° ± 4°	Varies between 0° and 10°	Varies between 1 and ~1.005; mostly not coaxial with $\epsilon_1$ ( $\epsilon_{xx}$ )
Case 6	MP3: Anisotropic medium ( $E=1.3E'$ )	BC3: axisymmetric extension ( $\epsilon_{zz} < \epsilon_{xx} = \epsilon_{yy}$ )	$\alpha_2$ is equal to $\alpha_1$ or 180°	0°	Varies between 1 and ~1.013; mostly not coaxial with $\epsilon_1$ ( $\epsilon_{xx}, \epsilon_{yy}$ )
Case 7	MP4: Anisotropic medium ( $E=1.2E'$ ) ( $\nu=1.1\nu'$ )	BC3: axisymmetric extension ( $\epsilon_{zz} < \epsilon_{xx} = \epsilon_{yy}$ )	$\alpha_2$ is equal to $\alpha_1$ or 180°	0°	Varies between 1 and ~1.013; mostly not coaxial with $\epsilon_1$ ( $\epsilon_{xx}, \epsilon_{yy}$ )
Case 8	MP5: Anisotropic medium ( $E=1.2E'$ ) ( $G=0.8G'$ )	BC3: axisymmetric extension ( $\epsilon_{zz} < \epsilon_{xx} = \epsilon_{yy}$ )	$\alpha_2$ is equal to $\alpha_1$ or 180°	0°	Varies between 1 and ~1.012; mostly not coaxial with $\epsilon_1$ ( $\epsilon_{xx}, \epsilon_{yy}$ )

Considering the notion that joints form perpendicular to the maximum principal (tensile) stress (Pollard and Aydin, 1988), these model results have important implications for our field observations.

### 6.3. Comparison between the model results and the field data

The field data (see Section 4) show that CBP (cross-bed package confined) joints trend roughly parallel to the dip direction of the cross-beds (Fig. 7). This relationship suggests that the plunge direction of the maximum principal tension responsible for the orientation of CBP joints varies with cross-bed orientation. In particular, the plunge direction ( $\alpha_2$ ) of the local maximum principal stress component is expected to coincide with the strike of the cross-beds ( $\alpha_1$ ) locally. For the boundary condition of axisymmetric extension ( $\epsilon_{xx} = \epsilon_{yy} > \epsilon_{zz}$ ) (Case 4, 6, 7 and 8), plunge direction ( $\alpha_2$ ) of  $\sigma_1$  remains the same (or 180° difference) as the strike of local cross-beds ( $\alpha_1$ ) when the latter varies. This is consistent with the field data of CBP joints. However, the plunge ( $\theta_2$ ) of  $\sigma_1$  remains constant at 0° (corresponding to vertical joints), but the dip angles of the CBP joints vary between 58° and 89° with a mean of 76°. These do not match well.

In contrast, the joint zone orientations do not change with changes in the cross-bed orientations. This outcome suggests that the plunge direction ( $\alpha_2$ ) of the maximum principal stress component responsible for the formation of the joint zones does not vary significantly in cross-beds of different orientations. For the model boundary condition, BC4 ( $\epsilon_{xx} > \epsilon_{yy} > \epsilon_{zz}$ ) (Case 5), the plunge direction ( $\alpha_2$ ) of  $\sigma_1$  does not vary significantly and remains around 90° and 270°. The plunge of  $\sigma_1$  ( $\theta_2$ ) is smaller than 10° (corresponding to a range of dip angles for potential joint planes larger than 80°). These results are in good agreement with the field data from the joint zones (Fig. 4).

## 7. Discussion

### 7.1. The notion of bed-normal joints

The notion that joints are commonly perpendicular to bedding is supported by many previous studies on jointing in sedimentary rocks (Hodgson, 1961; Price, 1966; Kulander et al., 1979; Gross and Engelder, 1995; Odonne et al., 2007). A commonly accepted interpretation for this notion is that sedimentary rocks are originally flat-lying and the regional principal stresses are orthogonal to bedding as dictated by the free surface during the formation of the joints before any tilting of the beds. Frictionless or very low friction across the bedding interfaces may also produce local principal stresses perpendicular to bedding (i.e. Cooke et al., 2000) even though the remote tensile principal stress is not vertical. However, in aeolian sandstones the cross-beds have an intrinsic dip angle and may have variable strikes due to the depositional processes (Hunter, 1977; Kocurek, 1991). Furthermore, there is no evidence for CBP joints formed associated with bed-parallel slip or dune-boundary slip in this study. The reason why joints formed at high-angle to bedding therefore remains intriguing from the perspective of classical view of the relationship between bedding and joint orientation.

The effect of bedding on the orientation of joints in different regions at different scales has been previously addressed by several classical studies of joints in sedimentary rocks. Hodgson (1961) noted that the systemic joints on Colorado Plateau were not affected by the cross-beds in the Navajo, Wingate, and DeChelly Sandstones. In contrast, Babcock (1973) found that “joints passing through cross-beds consistently change in dip from vertical to a dip normal to the cross-beds” in sandstones of

the lower Milk River Formation in southern Alberta. Nelson and Stearns (1977) based on their study of the regional fractures in the Lake Powell area of Utah and Arizona, concluded that the changes in strike of the regional fractures among different formations are due to mechanical anisotropies associated with large scale sedimentary structures. Winsor (1979) carried out a study of the regional fracture sets within the Delamerian fold belt in Australia and reported that two sets of fractures were in good correlation with the sedimentary anisotropy. From the preceding review, it is evident that bedding in general and cross-bedding in particular have been known to influence the orientation of joints in layered and cross-bedded rocks. However, most of these previous studies have pointed out the origin of this effect as “sedimentary anisotropy”, but few of them have analyzed and discussed the nature of the bedding associated anisotropy and its influence (or lack thereof) on the joint orientations within a mechanical framework.

The analysis in this study suggests that non-coaxiality between the directions of the principal stress and principal strain is in play for the fracture formation in anisotropic rocks. The notion of non-coaxial stress and strain has also been addressed by previous studies on deformation in different rock types (Cobbold, 1976; Platt and Vissers, 1980).

In the present study, when the maximum and intermediate strain components are the same (BC3:  $\epsilon_{xx} = \epsilon_{yy} > \epsilon_{zz}$ ), the model results (Fig. 12, Case 4, 6, 7 and 8) are in good agreement with the field data about the variation of strikes of CBP (cross-bed package confined) joints. Because the CBP joints have a broad variation in their orientation (from 0° to 80° and from 170° to 356° as shown in Fig. 4), the total extensional elastic strains accommodated by all the CBP joints within the horizontal plane are not very different, that is,  $\epsilon_{xx} \cong \epsilon_{yy}$ . The model results also suggest that when the horizontal stretching (maximum tensile strain component) is predominant along the east-west direction (BC4:  $\epsilon_{xx} > \epsilon_{yy} > \epsilon_{zz}$ ), the cross-bedding associated anisotropy will have an insignificant effect on the plunge direction of the maximum tensile stress component (Fig. 12a, Case 5). Therefore, the effect of cross-bedding associated anisotropy on the orientation of joint sets depends by and large on the boundary conditions: an axisymmetric extension ( $\epsilon_{xx} = \epsilon_{yy} > \epsilon_{zz}$ ) would amplify the effect of anisotropy on the joint orientation whereas a triaxial extension ( $\epsilon_{xx} > \epsilon_{yy} > \epsilon_{zz}$ ) would mitigate this effect. Thus the interplay between the mechanical boundary conditions and the rock properties, specifically cross-bed related anisotropy may produce different joint systems.

Previous studies (Meyers, 1999; Taylor et al., 1999) proposed that the joint zones of similar orientations in the Aztec Sandstone within the Valley of Fire State Park formed during the early stages of the east-west Miocene extension associated with the Basin and Range tectonism (e.g. Bohannon, 1983). Our field data and model results on joint zones are in agreement with these studies. The relatively consistent orientation and greater continuity of joint zones suggest that they might have formed at a different time and under a different loading regime than the CBP joints. Aydin and de Jossineau (2014) in their study of the temporal and spatial relationship between the normal faults and related joints versus strike-slip faults within Valley of Fire State Park, pointed out that a major reorganization of regional tectonic loading may have occurred to produce the observed sequence of the faulting events. Other authors using different methods and models concluded that temporal and spatial variations of the stresses (Zoback, 1989; Angelier et al., 1985) and strain patterns (Beard et al., 2010; Anderson et al., 2013) occurred in the Basin and Range province. In the absence of the relative timing between the formation of CBP joints and the history of the tectonic events referred to above, it is difficult to specify the tectonic origin corresponding to a strain boundary condition such

as BC3  $\epsilon_{xx} = \epsilon_{yy} > \epsilon_{zz}$ . However, it is plausible that such a boundary condition is associated with a temporal evolution of regional tectonic loading in the Valley of Fire region. Possible scenarios include the following: After the formation of the joint zones, tensile strains associated with the E–W horizontal stretching are relaxed resulting a strain relaxation in the E–W direction and a decrease of  $\epsilon_{xx}$ , which may lead to the change of boundary condition from true triaxial ( $\epsilon_{xx} > \epsilon_{yy} > \epsilon_{zz}$ ) to axisymmetric BC3 ( $\epsilon_{xx} = \epsilon_{yy} > \epsilon_{zz}$ ). Although we do not present any evidence for a particular scenario, we believe that the variation of the driving stresses and strains in a broad area like the Basin and Range province during a large geological span is quite plausible.

The dip angles of CBP joints varying between  $58^\circ$  and  $89^\circ$ , which does not match well with the model results predicting a  $90^\circ$  dip angle. To resolve this discrepancy, future work is needed to investigate the range of elastic properties in detail and incorporate them into our model. P-wave velocity measurements (Section 5) suggest that a difference exists between the two orthogonal directions within the bedding plane. Therefore, material properties other than transverse isotropy, for example, orthotropic system, are worth further study in the cross-bedded sandstones. In addition, the relation between the mechanical strength of opening-mode fracture formation and the bedding orientation may also be an important factor. To this end, modeling studies using the strength of localized compaction such as weak (favorable) or strong (unfavorable) on the distribution and orientations of compaction bands are promising (Deng and Aydin, 2015). It is likely that the opening-mode fracture formation can also be defined as a function of cross-bed orientation.

### 7.2. Microstructure attributes affecting the degree of anisotropy

The measured Young's modulus  $E'$  of Aztec Sandstone samples (Section 5.1) is roughly similar to those of other porous sandstones (Obert and Duvall, 1967). In contrast, Poisson's ratio  $\nu$  are relatively large (0.35–0.37) comparing to the "typical value" of 0.25 (Bieniawski, 1984), but are consistent with similar sandstones that are poorly-cemented (Dvorkin and Nur, 1996).

Flodin et al. (2003) measured the difference between the petrophysical properties of the lower, middle and upper members of the Aztec Sandstone to explain the different degrees of the presences of deformation bands and joints in these members. They concluded that porosity appears to be the major factor controlling the deformation style. They investigated mainly the ultrasonic velocities perpendicular to bedding, and measured velocities in two directions only for few samples. The P-wave anisotropy calculated from the unpublished data from Flodin (2003) agrees well with our measurements. In our study, efforts have been made to measure the stiffness anisotropy (difference between  $E'$  and  $E$  in addition to the P-wave velocity). However, because the samples are poorly consolidated and fragile, the surfaces oriented perpendicular to bedding planes are difficult to be prepared exactly parallel or within the required limits. We therefore propose that the static set-up is not appropriate to measure the elastic anisotropy in poorly consolidated granular rocks, such as the middle member of the Aztec Sandstone.

P-wave anisotropy (Fig. 10a) measured from different samples show a wide range of values (–5% to 36%). Because the samples were collected from different locations across multiple dunes and from different cross-beds within a single dune, such variations in the measured P-wave anisotropy are probably related to the textural differences among the samples collected from different depositional strata (Hunter, 1977; Kocurek, 1991). For instance, samples 6B and 6C have the highest measured degree of P-wave anisotropies at 21% and 36%, respectively (see Fig. 10). They were collected from the

bottom sets (wind-ripple strata) right above the dune boundary (Fig. 1, inset) where a concentration of fine and ultra fine materials occurs (Deng and Aydin, 2012, Fig. 9c therein), forming thinly bedded (<1 mm) pin-stripe laminations (see Fryberger and Schenk, 1988 for the details of the definition). Compared with other samples from relatively thicker beds collected from the foresets (grainflow strata), such a thinly laminated texture will certainly have a greater degree of P-wave anisotropy (Melia and Carlson, 1984). In comparison to samples 6B and 6C, the measured P-wave anisotropy of sample 2C is nearly zero. This state might be due to the individual bed thickness that is larger than the diameter (13 mm) of the transducers and therefore the measurement gives a single-layer response. Alternatively, relatively low P-wave anisotropy might also be due to local heterogeneity of this sample. For instance, the measured velocities of 2C appear to be an outlier for the overall data set (Fig. 10a). However, comparing to the thickness (about 25 mm) of the samples tested in the laboratory, the thickness of the cross-bed packages (CBP) (Figs. 3 and 5) in the field is much larger. The cross-bed package-associated anisotropy is likely greater than the tested samples that probably consist of only a limited number of beds in thickly bedded sequences. Besides the layered (laminated) texture, the other microstructure attributes of aeolian sandstones, such as grain shape, alignment, and orientation (Schwarzacher, 1951; Mazzullo et al., 1986) might also contribute to the P-wave anisotropy.

It is interesting to point out that cross-beds exert a strong influence on the CBP joints and the dune boundaries have a strong influence on the joint zones as evidenced by the former being confined in cross-bed packages whereas the latter are generally truncated at the dune boundaries. Compared to the bedding interfaces that bound the CBP joints, dune boundaries can be considered as boundaries of a hierarchy associated with a higher degree of inhomogeneity including fine-grained interdune deposits (e.g. Brookfield, 1977). This difference suggests that boundaries of various hierarchies exert different influences on joint sets formation under different loading conditions and/or mechanisms. This hierarchy reflects various degrees of the interface influences on joint formation in the aeolian sandstones is not well understood and remains to be further investigated.

### 7.3. Potential impact on fluid flow

The field data have important implications for fluid flow through aeolian sandstones in reservoirs and aquifers. Unfilled joints provide flow paths for fluids and gas. Therefore, their distribution and geometric complexities are crucial to reservoir dynamics. Given the good agreement between our model results and field data, the model can be used for predicting joint orientations in other deformed aeolian sandstones in the subsurface.

## 8. Conclusions

We report the relationship between cross-bed orientation and the orientation of different categories of joints in the Jurassic aeolian Aztec Sandstone cropping out in the Valley of Fire State Park. We interpret that joint zones and cross-bed package confined joints have different histories and different driving mechanisms. The data show that cross-bed package confined joints are generally at a high-angle to bedding and are trending roughly parallel to the dip direction of the cross-beds. In comparison, the roughly N–S trending joint zones do not change orientation with changes in cross-bed orientations, but are frequently truncated by the dune boundaries. In light of these observations, cross-beds and the associated anisotropy exert a strong control on the formation and orientation of the cross-bed package confined joints, and the dune

boundaries have significant impact on the propagation and termination of joint zones.

Assuming transversely isotropic stress–strain relations for the Aztec Sandstone samples, the statically measured Young's modulus  $E$  are moderate (4.8 GPa–6.5 GPa) and the Poisson's ratio ( $\nu'$ ) are relatively large (0.35–0.37). The measured P-wave velocities parallel and perpendicular to bedding from 11 samples provide an average P-wave anisotropy of slightly larger than 13%. P-wave velocities parallel to bedding but in two orthogonal directions were measured from 5 samples, and varied by roughly  $\pm 5\%$ . Based on the measured P-wave anisotropy, a three dimensional stress–strain model from the generalized Hooke's Law was used to analyze deformation of cross-bedded sandstone as a transversely isotropic medium.

For different strain boundary conditions, a majority of the model results are in qualitative agreement with the field relations between joint sets and cross-beds. The results also suggest that uniaxial extension ( $\epsilon_{zz} > \epsilon_{xx} = \epsilon_{yy} = 0$ ) and axisymmetric extension ( $\epsilon_{xx} = \epsilon_{yy} < \epsilon_{zz}$  and  $\epsilon_{xx} = \epsilon_{yy} > \epsilon_{zz}$ ) would amplify the influence of cross-bedding associated anisotropy on the joint orientation, whereas a triaxial extension ( $\epsilon_{xx} > \epsilon_{yy} > \epsilon_{zz}$ ) would mitigate this influence. Therefore, even though the temporal relationships between different joint systems and different types of extensional boundary strains are not well established, it is likely that the Valley of Fire region has been subjected to different loading conditions throughout the Miocene time to account for the different paths of the joint zones and cross-bed package confined joints. The potential implications of joints with significantly different orientations and geometries forming in response to variations in the boundary conditions and their interplay with the rock anisotropy is intriguing and provide a fertile ground for future studies.

## Acknowledgments

We thank Rui Jiang for his assistance in the field. Special thanks to Gary Mavko for the discussions and comments on the rock anisotropy. We also thank the official reviewers, Ryan Shackleton and Michele Cooke, for their constructive comments that improved the manuscript. The Editor of Journal of Structural Geology, Bill Dunne's proofreading and editing is much appreciated. This material is based upon work supported by the U.S. Department of Energy Office of Science, Office of Basic Energy Sciences, Geosciences Research Program under Award Number DE-FG02-04ER15588. Last but not the least, we are grateful to the Valley of Fire State Park personnel for their permit to do field work and to collect samples within the Park.

## References

- Anderson, R.E., Beard, L.S., Mankinen, E.A., Hillhouse, J.W., 2013. Analysis of Neogene deformation between Beaver, Utah, and Barstow, California: suggestions for altering the extensional paradigm. In: Anderson, R.E. (Ed.), *Neogene Deformation between Central Utah and the Mojave Desert*: Geological Society of America Special Paper 499, pp. 1–67. [http://dx.doi.org/10.1130/2013.2499\(01\)](http://dx.doi.org/10.1130/2013.2499(01)).
- Aydin, A., de Jossineau, G., 2014. The relationship between normal and strike-slip faults in valley of Fire State Park, Nevada, and its implications for stress rotation and partitioning of deformation in the east-central Basin and Range. *J. Struct. Geol.* 63, 12–26.
- Angelier, J., Colletta, B., Anderson, R.E., 1985. Neogene paleostress changes in the basin and range: a case study at Hoover Dam, Nevada–Arizona. *Geol. Soc. Am. Bull.* 96, 347e361.
- Babcock, E.A., 1973. Regional jointing in southern Alberta. *Can. J. Earth Sci.* 10 (12), 1769–1781.
- Bai, T., Maerten, L., Gross, M.R., Aydin, A., 2002. Orthogonal cross joints: do they imply a regional stress rotation? *J. Struct. Geology* 24 (1), 77–88.
- Beard, L.S., Campagna, D.J., Anderson, R.E., 2010. Geometry and kinematics of the eastern Lake Mead fault system in the Virgin Mountains, Nevada and Arizona. In: Umhoefer, P.J., Beard, L.S., Lamb, M.A. (Eds.), *Miocene Tectonics of the Lake Mead Region, Central Basin and Range*: Geological Society of America Special Paper 463, pp. 243–274. [http://dx.doi.org/10.1130/2010.2463\(11\)](http://dx.doi.org/10.1130/2010.2463(11)).
- Bieniawski, Z.T., 1984. *Rock Mechanics Design in Mining and Tunneling*. A.A. Balkema, Rotterdam.
- Bohannon, R.G., 1983. Mesozoic and Cenozoic tectonic development of the Muddy, North Muddy, and northern Black Mountains, Clark County, Nevada: Boulder–Colorado. *Geol. Soc. Am. Mem.* 157, 125–148.
- Brookfield, M.E., 1977. The origin of bounding surfaces in ancient eolian sandstones. *Sedimentology* 24, 303–332.
- Cobbold, P., 1976. Mechanical effects of anisotropy during large finite deformations. *Bull. la Société géologique Fr.* 6, 1497–1510.
- Cooke, M.L., Simo, J.A., Underwood, C.A., Rijken, P., 2006. Mechanical stratigraphic controls on fracture patterns within carbonates and implications for groundwater flow. *Sediment. Geol.* 184 (3), 225–239.
- Cooke, M.L., Mollema, P.N., Pollard, D.D., Aydin, A., 2000. Interlayer slip and joint localization in East Kaibab Monocline, Utah: field evidence and results from numerical modelling. *Spec. Pub. Geol. Soc. Lond.* 169, 23–50.
- Deng, S., Aydin, A., 2012. Distribution of compaction bands in 3D in an aeolian sandstone: the role of cross-bed orientation. *Tectonophysics* 574–545, 204–218.
- Deng, S., Aydin, A., 2015. The strength anisotropy of localized compaction: a model for the role of the nature and orientation of cross-beds on the orientation and distribution of compaction bands in 3-D. *J. Geophys. Res. Solid Earth* 120. <http://dx.doi.org/10.1002/2014JB011689>.
- Dvorkin, J., Nur, A., 1996. Elasticity of high-porosity sandstones: theory for two North Sea data sets. *Geophysics* 61 (5), 1363–1370.
- deJossineau, G., Aydin, A., 2007. The evolution of the damage zone with fault growth in sandstone and its multiscale characteristics. *J. Geophys. Res. Solid Earth* (1978–2012) 112 (B12).
- Eichhubl, P., Taylor, W.L., Pollard, D.D., Aydin, A., 2004. Paleo-fluid flow and deformation in the Aztec Sandstone at the Valley of Fire, Nevada—Evidence for the coupling of hydrogeologic, diagenetic, and tectonic processes. *Geol. Soc. Am. Bull.* 116 (9–10), 1120–1136.
- Flodin, E.A., 2003. *Structural Evolution, Petrophysics, and Large-scale Permeability of Faults in Sandstone, Valley of Fire, Nevada* (Ph.D. thesis). Stanford University, California, p. 180.
- Flodin, E.A., Prasad, M., Aydin, A., 2003. Petrophysical constraints on deformation styles in Aztec Sandstone, southern Nevada, USA. *Pure Appl. Geophys.* 160 (9), 1589–1610.
- Flodin, E.A., Aydin, A., 2004. Evolution of a strike-slip fault network, Valley of Fire, southern Nevada. *Geol. Soc. Am. Bull.* 116, 42–59.
- Fryberger, S.G., Schenk, C.J., 1988. Pin stripe lamination: a distinctive feature of modern and ancient eolian sediments. *Sediment. Geol.* 55, 1–15.
- Gross, M.R., 1995. Fracture partitioning: failure mode as a function of lithology in the Monterey Formation of coastal California. *Geol. Soc. Am. Bull.* 107 (7), 779–792.
- Gross, M.R., Engelder, T., 1995. Fracture strain in adjacent units of the Monterey Formation: scale effects and evidence for uniform displacement boundary conditions. *J. Struct. Geol.* 17, 1303–1318.
- Hancock, P.L., 1985. Brittle microtectonics: principle and practice. *J. Struct. Geol.* 7, 437–457.
- Helgeson, D.E., Aydin, A., 1991. Characteristics of joint propagation across layer interfaces in sedimentary rocks. *J. Struct. Geol.* 13, 897–911.
- Hill, R.E., 1989. *Analysis of Deformation Bands in the Aztec Sandstone, Valley of Fire State Park, Nevada* (Master's thesis). University of Nevada, Las Vegas.
- Hodgson, R.A., 1961. Regional Study of Jointing in Comb Ridge–Navajo Mountain Area, vol. 45. American Association of Petroleum Geologists Bulletin, Arizona and Utah, pp. 1–38.
- Hunter, R.E., 1977. Basic types of stratification in small eolian dunes. *Sedimentology* 24 (3), 361–387.
- Kocurek, G., 1991. Interpretation of ancient eolian sand dunes. *Annu. Rev. Earth Planet. Sci.* 19, 43.
- Kulander, B.R., Barton, C.C., Dean, S.L., 1979. *The Application of Fractography to Core and Outcrop Fracture Investigations*. US Department of Energy, Morgantown Energy Technology Center, Morgantown, W.Va.
- Laubach, S.E., Olson, J.E., Gross, M.R., 2009. Mechanical and fracture stratigraphy. *AAPG Bull.* 93 (11), 1413–1426.
- Lekhnitskii, S.G., 1963. *Theory of Elasticity of an Anisotropic Elastic Body*. Holden-Day.
- Lockner, D.A., Stanchits, S.A., 2002. Undrained poroelastic response of sandstones to deviatoric stress change. *J. Geophys. Res.* 107 (B12), 2353. <http://dx.doi.org/10.1029/2001JB001460>.
- Marzolf, J.E., 1983. Changing wind and hydrologic regimes during deposition of the Navajo and Aztec Sandstones, Jurassic (?). South. United States. *Dev. Sedimentol.* 38, 635–660.
- Mavko, G., Mukerji, T., Dvorkin, J., 2009. *The Rock Physics Handbook: Tools for Seismic Analysis of Porous Media*. Cambridge University Press, p. 511.
- Mazzullo, J., Donald, S., Cunningham, D., 1986. The effects of eolian sorting and abrasion upon the shapes of fine quartz sand grains. *J. Sediment. Petrol.* 56, 45–56.
- McKee, E.D., Bigarella, J.J., 1979. Ancient sandstones considered to be eolian. A study of global sand seas. In: McKee, E.D. (Ed.), *US Geol. Surv., Prof. Pap.* vol. 1052, pp. 187–238.
- Melia, P.J., Carlson, R.L., 1984. An experimental test of P-wave anisotropy in stratified media. *Geophysics* 49 (4), 374–378.
- Myers, R.D., 1999. *Structure and Hydraulics of Brittle Faults in Sandstone* (Ph.D. thesis). Stanford University, Stanford, California, p. 176.
- Myers, R., Aydin, A., 2004. The evolution of faults formed by shearing across joint zones in sandstone. *J. Struct. Geol.* 26, 947–966.

- Narr, W., 1991. Fracture density in the deep subsurface: techniques with application to point Arguello oil field (1). *AAPG Bull.* 75 (8), 1300–1323.
- Nelson, R.A., Stearns, D.W., 1977. Interformational control of regional fracture orientations. In: *Rocky Mountain Associate of Geologists Symposium*.
- Obert, L., Duvall, W.L., 1967. *Rock Mechanics and the Design of Structures in Rock*.
- Odonne, F., Lézin, C., Massonnat, G., Escadeillas, G., 2007. The relationship between joint aperture, spacing distribution, vertical dimension and carbonate stratification: an example from the Kimmeridgian limestones of Pointe-du-Chay (France). *J. Struct. geol.* 29 (5), 746–758.
- Platt, J.P., Vissers, R.L.M., 1980. Extensional structures in anisotropic rocks. *J. Struct. Geol.* 2 (4), 397–410.
- Pollard, D.D., Aydin, A., 1988. Progress in understanding jointing over the past century. *Geological Soc. Am. Bull.* 100 (8), 1181–1204.
- Pollard, D.D., Fletcher, R.C., 2005. *Fundamentals of Structural Geology*. Cambridge, p. 500.
- Porter, M.L., 1987. Sedimentology of an ancient erg margin: the Lower Jurassic Aztec Sandstone, southern Nevada and southern California. *Sedimentology* 34 (4), 661–680.
- Price, N.J., 1966. *Fault and Joint Development in Brittle and Semi-brittle Rock*. Pergamon Press, New York, p. 568.
- Rutter, E.H., 1998. Use of extension testing to investigate the influence of finite strain on the rheological behaviour of marble. *J. Struct. Geol.* 20 (2), 243–254.
- Schwarzacher, W., 1951. Grain orientation in sands and sandstones. *J. Sediment. Petrol.* 21.
- Sternlof, K.R., 2006. *Structural Geology, Propagation Mechanics and Hydraulic Effects of Compaction Bands in Sandstone* (Ph.D. thesis). Stanford University, Stanford, California, p. 214.
- Taylor, W.L., Pollard, D.D., Aydin, A., 1999. Fluid flow in discrete joint sets: field observations and numerical simulations. *J. Geophys. Res.* 104, 28,983–29,006.
- Thomsen, L., 1986. Weak elastic anisotropy. *Geophysics* 51 (10), 1954–1966.
- Winsor, C.N., 1979. The correlation of fracture directions with sediment anisotropy in folded rocks of the Delamerian fold belt at Port Germein gorge, South Australia. *J. Struct. Geol.* 1 (3), 245–254.
- Zoback, M.L., 1989. State of stress and modern deformation of the northern Basin-and Range province. *J. Geophys. Res.* 94, 7105–7128.